

Benchmark of FEM, Waveguide and FDTD Algorithms for Rigorous Mask Simulation

Sven Burger^{ab}, Roderick Köhle^c, Lin Zschiedrich^{ab}, Weimin Gao^d,
Frank Schmidt^{ab}, Reinhard März^{be}, Christoph Nölscher^f

^a Zuse Institute Berlin, Takustraße 7, D-14 195 Berlin, Germany
DFG Forschungszentrum MATHEON, Straße des 17. Juni 136, D-10 623 Berlin, Germany

^b JCMwave GmbH, Haarer Straße 14a, D-85 640 Putzbrunn, Germany

^c Infineon Technologies AG, MP PD CS ATS,
Balanstraße 73, D-81 541 München, Germany

^d Sigma-C Software AG, Thomas-Dehler-Straße 9, D-81 737 München, Germany

^e Infineon Technologies AG, COM CAL D TD RETM PI,
Balanstraße 73, D-81 541 München, Germany

^f Infineon Technologies SC300 GmbH&Co OHG, IFD P300LM,
Königsbrücker Straße 180, D-01 099 Dresden, Germany

Copyright 2005 Society of Photo-Optical Instrumentation Engineers.

This paper has been published in Proc. SPIE **5992**, pages 378-389 (2005), (*25th Annual BACUS Symposium on Photomask Technology*, J. T. Weed, P. M. Martin, Eds.) and is made available as an electronic reprint with permission of SPIE. One print or electronic copy may be made for personal use only. Systematic or multiple reproduction, distribution to multiple locations via electronic or other means, duplication of any material in this paper for a fee or for commercial purposes, or modification of the content of the paper are prohibited.

ABSTRACT

An extremely fast time-harmonic finite element solver developed for the transmission analysis of photonic crystals was applied to mask simulation problems. The applicability was proven by examining a set of typical problems and by a benchmarking against two established methods (FDTD and a differential method) and an analytical example. The new finite element approach was up to 100× faster than the competing approaches for moderate target accuracies, and it was the only method which allowed to reach high target accuracies.

Keywords: Photomask simulation benchmark, photolithography, phase shift mask, FEM, FDTD

1. INTRODUCTION

The complexity of modern photolithography makes extensive simulations indispensable.¹ Modern lithography simulators include modules describing illumination, transfer of the optical field through the mask and aberrating optical system of the lithographic equipment, the propagation inside the photoresist, the processes leading to the resist image and – in advanced systems – the etching processes leading to the etched image. After nearly two decades of lithography simulation, most of the modules along the simulation chain have attained a high degree of maturity. However, the simulation of light propagation through phase shift masks, also applied for the stand-alone analysis of masks and mask tolerances, is still challenging in terms of both computational time and accuracy of the results.

The computation of the print image of a whole chip remains extremely demanding although approximations, multi-threading and even hardware accelerators are applied to reduce the runtime of simulations. Rigorous

Corresponding author: S. Burger

URL: <http://www.zib.de/nano-optics/>

Email: burger@zib.de

simulations are restricted today to small areas and even those simulations suffer from the high computational effort. At the same time, the progress on the semiconductor roadmap forces the need of rigorous 3D simulations, in particular also for alternating and attenuated phase masks. Experimental investigations of the polarization effects in Hyper NA immersion lithography² support this assertion. Further, the demand to assess the process stability by exploring several dose/defocus conditions in the process window sharpens the shortage of computational resources.

Keeping this background in mind, we evaluated a frequency-domain finite-element method (FEM) solver for Maxwell's equations which has been successfully applied to a wide range of electromagnetic field computations including optical and microwave waveguide structures, surface plasmons, and nano-structured materials. In addition, the activity was motivated by a preceding, successful benchmarking³ against MPB, a widely used and highly sophisticated plane-wave solver used for the Bloch mode analysis of photonic crystals.⁴

In this contribution, the new FEM solver is benchmarked against an analytical result which is fairly realistic for lithography, and against two competing algorithms commonly applied for the simulation of "thick" phase masks. For the simulation of periodic mask patterns in lithography the most prominent rigorous simulation methods include the finite-difference time domain algorithm (FDTD)^{5,6} and the modal methods such as the differential method^{7,8} or the closely related rigorous coupled wave analysis (RCWA).⁹ The methods differ in the way Maxwell's equations are numerically solved and how the boundary conditions of the interfaces to the unbound regions above and below the mask are established. We will give a brief description of the algorithms to give a rough idea about the relevant parameters influencing simulation speed and accuracy in the next paragraph. A brief description of FEM will be given in Section 2.

The FDTD approach discretizes Maxwell's equations in both time and space and solves the scattering problem by simulating the field evolution through time until the time-harmonic steady-state solution is reached. The interfaces to the unbound regions are formed by perfectly matched layers (PML). Space and time discretization are interdependent ("magic steps"). Speed and accuracy of the simulation depend on the space and time discretization, the total time period and on the PML parameters. The differential method describes the propagating fields inside the mask by a plane wave expansion. Maxwell's equations are thus converted into a system of linear ordinary differential equations (ODEs) relating the scattered waves at the upper and lower mask interfaces. Speed and accuracy depend on the number of plane waves and on the resolution used for ODE integration.

This paper is organized as follows: Section 2 introduces the concept of the FEM solver. Section 3 presents several proofs of applicability including 3D simulations, 2D simulations for light scattering off line masks under conical incidence, and adaptive refinement of FEM meshes. Section 4 shows benchmark results of the three different solvers for a mask with dense lines and spaces illuminated at normal incidence. Section 5 verifies the accuracy of the FEM solver by examining a closely related toy example offering an analytical solution.

2. FREQUENCY-DOMAIN FEM ANALYSIS FOR PHOTOMASK SIMULATIONS

This paper considers light scattering off a system which is periodic in the x - and y -directions and is enclosed by homogeneous substrate (at z_{sub}) and superstrate (at z_{sup}) which are infinite in the $-$, resp. $+$ z -direction. Light propagation in the investigated system is governed by Maxwell's equations where vanishing densities of free charges and currents are assumed. The dielectric coefficient $\varepsilon(\vec{x})$ and the permeability $\mu(\vec{x})$ of the considered photomasks are periodic and complex, $\varepsilon(\vec{x}) = \varepsilon(\vec{x} + \vec{a})$, $\mu(\vec{x}) = \mu(\vec{x} + \vec{a})$. Here \vec{a} is any elementary vector of the periodic lattice.¹⁰ For given primitive lattice vectors \vec{a}_1 and \vec{a}_2 an elementary cell $\Omega \subset \mathbb{R}^3$ is defined as $\Omega = \{\vec{x} \in \mathbb{R}^2 \mid x = \alpha_1 \vec{a}_1 + \alpha_2 \vec{a}_2; 0 \leq \alpha_1, \alpha_2 < 1\} \times [z_{sub}, z_{sup}]$. A time-harmonic ansatz with frequency ω and magnetic field $\mathbf{H}(\vec{x}, t) = e^{-i\omega t} \mathbf{H}(\vec{x})$ leads to the following equations for $\mathbf{H}(\vec{x})$:

- The wave equation and the divergence condition for the magnetic field:

$$\nabla \times \frac{1}{\varepsilon(\vec{x})} \nabla \times \mathbf{H}(\vec{x}) - \omega^2 \mu(\vec{x}) \mathbf{H}(\vec{x}) = 0, \quad \vec{x} \in \Omega, \quad (1)$$

$$\nabla \cdot \mu(\vec{x}) \mathbf{H}(\vec{x}) = 0, \quad \vec{x} \in \Omega, \quad (2)$$

- Transparent boundary conditions at the boundaries to the substrate (at z_{sub}) and superstrate (at z_{sup}), $\partial\Omega$, where \mathbf{H}^{in} is the incident magnetic field (plane wave in this case), and \vec{n} is the normal vector on $\partial\Omega$:

$$\left(\frac{1}{\varepsilon(\vec{x})}\nabla \times (\mathbf{H} - \mathbf{H}^{in})\right) \times \vec{n} = DtN(\mathbf{H} - \mathbf{H}^{in}), \quad \vec{x} \in \partial\Omega. \quad (3)$$

The DtN operator (Dirichlet-to-Neumann) is realized with the PML method.¹¹ This is a generalized formulation of Sommerfeld's radiation condition; it can be realized alternatively by the Pole condition method.¹²

- Periodic boundary conditions for the transverse boundaries, $\partial\Omega$, governed by Bloch's theorem¹⁰:

$$\mathbf{H}(\vec{x}) = e^{i\vec{k}\cdot\vec{x}}\mathbf{u}(\vec{x}), \quad \mathbf{u}(\vec{x}) = \mathbf{u}(\vec{x} + \vec{a}), \quad (4)$$

where the Bloch wavevector $\vec{k} \in \mathbb{R}^3$ is defined by the incoming plane wave \mathbf{H}^{in} .

Similar equations are found for the electric field $\mathbf{E}(\vec{x}, t) = e^{-i\omega t}\mathbf{E}(\vec{x})$; these are treated accordingly.

The finite-element method solves Eqs. (1) – (4) in their weak form, i.e., in an integral representation. The computational domain is discretized with triangular (2D) or tetrahedral (3D) patches. The functional spaces are discretized using Nedelec's edge elements, which are vectorial functions of polynomial order (typically second order) defined on the triangular or tetrahedral patches.¹³ In a nutshell, FEM can be explained as expanding the field corresponding to the exact solution of Equation (1) in the basis given by these elements. This leads to a large sparse matrix equation (algebraic problem). For details on the weak formulation, the choice of Bloch-periodic functional spaces, the FEM discretization, and our implementation of the PML method we refer to previous works.^{11, 14, 15} To solve the algebraic problem on a personal computer either standard linear algebra decomposition techniques (LU-factorization, e.g., package PARDISO¹⁶) or iterative methods¹⁷ are used, depending on problem size. Due to the use of multi-grid algorithms, the computational time and the memory requirements grow linearly with the number of unknowns.

From the users's point of view, the FEM approach presented here offers the following advantages:

- The expansion into localized functions (shared with any FEM and FD approach) is adequate for step index profiles occuring in masks.
- The flexibility of triangulations (shared with any FEM approach) allows for the simulation of mask imperfections such as sloped etch profiles and for adaptive mesh-refinement strategies leading to faster convergence.
- The frequency domain approach (shared with any PW method) is adequate for monochromatic or nearly monochromatic illumination.
- Edge elements provide "built-in" dielectric boundary conditions crucial for a high precision simulation of step index profiles.
- The mathematical structure of the algebraic problem allows for the use of very efficient numerical solvers, i.e., numerical methods where the computational effort grows linearly with the number of unknowns only.
- The FEM discretization is characterized by two parameters, the mesh width h and the thickness of the PML layer ρ . It is mathematically proven that the FEM approach converges with a fixed convergence rate towards the exact solution of Maxwell-type problems for mesh width $h \rightarrow 0$, and $\rho \rightarrow \infty$.^{13, 18} This allows to easily check whether the attained results can be trusted.

These advantages result not only in an increased attainable accuracy, but – via the reduced number of unknowns – also in a significantly reduced computational effort at moderate target accuracies required for lithography simulation. The investigated FEM solver JCMharmony includes adaptive grid refinement, higher order, 3D Nedelec elements, advanced periodic and transparent boundary conditions and flexible interfaces to the drivers and for postprocessing. Typical computation times for 3D problems are 30 seconds for problems with $N \approx 30\,000$ unknowns and 5 minutes for problems with $N \approx 150\,000$ unknowns solved on an actual standard 64 bit personal computer (*AMD Opteron*). Typical computation times for 2D problems are given in Table 2.

3. FEATURES OF THE FEM SOLVER

The range of applications of the FEM approach was examined by means of several characteristic tasks in mask simulation.

3.1. Conical Incidence

Here we investigate line masks illuminated under conical incidence (i.e., oblique incidence with respect to both mask plane and grating lines). This is crucial for the accurate simulation of off-axis source points for dipole, quadrupole or annular illumination. Figure 1 shows the schematics the geometry of the problem. The geometrical, material and source parameters are given in Table 1 (data set 1). The geometry does not depend on the y -component, therefore Eqn. (1) reduces to a simpler equation where 2D differential operators act on the 3D electric, resp. magnetic fields. Nevertheless, the problem is simulated without any approximations.

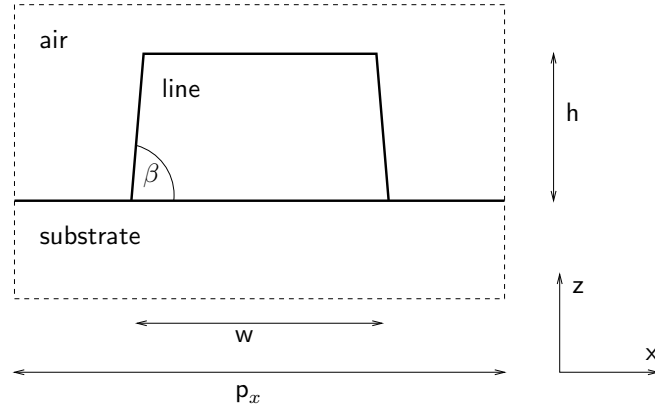


Figure 1. Schematics of the geometry of a periodic linemask: The computational domain consists of a line of width w (at center of the line), height h and sidewall angle β , on a substrate material SiO_2 , surrounded by air. The geometry is periodic in x -direction with a pitch of p_x and it is independent on the y -coordinate. The refractive indices of the different present materials are denoted by n_1 (line), n_2 (substrate) and n_3 (air), $n_3 = 1.0$.

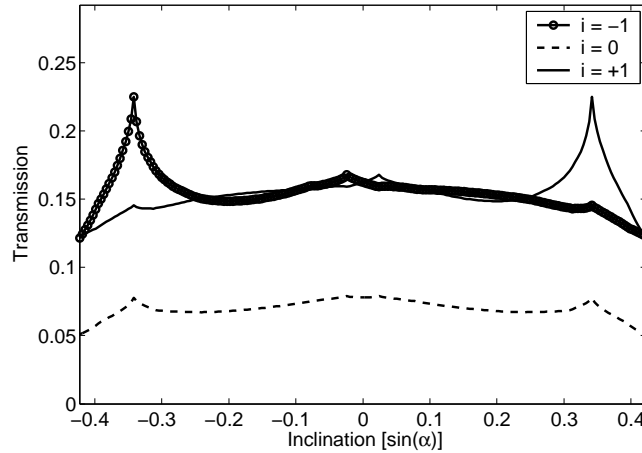


Figure 2. Diffraction of a plane wave under conical incidence. Intensities of the transmission to the central diffraction orders ($T = |\vec{A}(\vec{k}_i)|^2, i = -1, 0, +1$) in dependence on the inclination angle α , where $\vec{A}(\vec{k}_i)$ is defined in Eqn. (5). The angle of rotation is constantly $\theta = 20^\circ$.

The performance of the FEM solver is demonstrated by a parameter scan for varied inclination angle α of the source (S -polarization). The wavevector \vec{k} of the incident plane wave is attained by a rotation of the vector

parameter	data set 1	data set 2	data set 3	data set 4
p_x	400 nm	200 – 800 nm	400 nm	800 nm
w	200 nm	$p_x/2$	200 nm	400 nm
β	86°		90°	
α	$-25^\circ \dots +25^\circ$		0°	
Θ	20°		0°	
λ_0	193.0 nm			
h	65.4 nm			
n_1	$2.52 + 0.596i$			
n_2	1.56306			

Table 1. Parameter settings for the simulations in Sections 3.1 (data set 1), 3.2 (set 2), 3.3 (set 3) and 4 (set 4).

$(0, 0, 2\pi/\lambda)$ (where $\lambda = \lambda_0/n_2$, vacuum wavelength λ_0 , refractive index n_2) around the y -axis by the inclination angle α and a subsequent rotation around the z -axis by the rotation angle Θ . In this scan we fix the rotation, $\Theta = 20^\circ$ and vary the inclination, $\alpha = -25 \dots 25$, further parameters are given in Table 1. This yields an incident wave vector which is scanned from $\vec{k} \approx (-2.021, -0.736, 4.612)10^7/\text{m}$ to $\vec{k} \approx (2.021, 0.736, 4.612)10^7/\text{m}$. Figure 2 shows the normalized magnitude of the Fourier coefficients corresponding to the zero and first diffraction orders of the scattered light field in dependence on the angle of incidence. A typical computation time for a single data point in this scan was 15 sec ($N \approx 3 \times 10^4$ unknowns, adaptive grid refinement, computation on a personal computer/Intel Pentium IV, 2.5 GHz), resulting in a total time of roughly 1 h for the scan with 200 data points.

3.2. Degree of Polarization of Light Transmitted through a Line Mask

We have performed a scan over different geometrical parameters by varying the pitch and the linewidth of a line-mask. Geometrical, material and source parameters are again given in Fig. 1 and in Table 1 (data set 2). Since the plane of incidence is normal to the grating lines ($k_y = 0$), TE- and TM-polarization is supported, i.e., the problem becomes scalar.

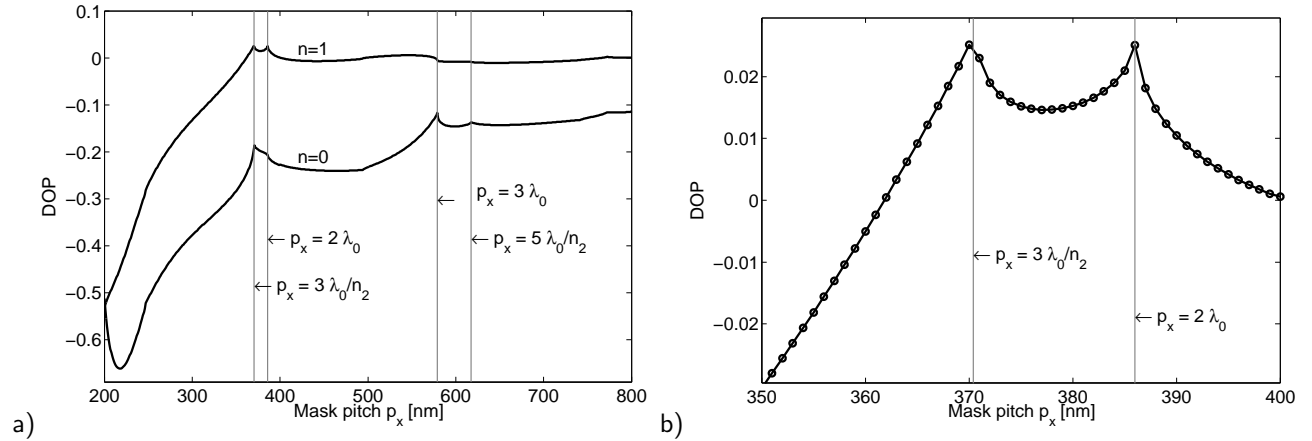


Figure 3. (a) Degree of polarization in dependence on mask pitch (p_x) for light diffracted to the zero ($i = 0$) and first ($i = 1$) diffraction order. Several strong Wood's anomalies are indicated at $p_x = N\lambda$. (b) Enlargement of a detail.

Figure 3 shows the degree of polarization of the zero and first transmitted diffraction orders, defined as $DOP = (I_{TE} - I_{TM})/(I_{TE} + I_{TM})$ in dependence on the pitch p_x . The strong Wood anomalies,⁷ some of which are also verified by Teuber et al.,² are caused by the excitation of waves traveling along the mask surface. We have constructed transparent boundary conditions for the whole range of investigated pitches, including 'regular' regions where the transmitted diffraction orders correspond to plane waves with a nonzero z -component

of the wavevector and regions close to Wood’s anomalies where certain diffraction orders cannot propagate as plane waves anymore. We are currently implementing an adaptive strategy for the PML implementation of the transparent boundary conditions in order to automatically account for such effects.

The average computation time for a single data point in this scan was about 3.5 sec ($N \approx 1 - 4 \times 10^4$ unknowns, depending on geometry size, yielding a relative error of the diffraction intensities of less than 1%; computation on a personal computer/Intel Pentium IV, 2.5 GHz), resulting in a total time of roughly 75 min for the scan with 1200 data points. Similar results are obtained with the solvers SOLID E and Delight (see Section 4), however, the Wood’s anomalies are not or less accurately resolved.

3.3. Adaptive Grid Refinement

By refining the resolution of the geometry-triangulation the accuracy of the solution is increased. FEM-solvers use as a standard a *regular* grid refinement, i.e., in 3D *each* tetrahedron of the discretization is refined to eight smaller tetrahedra, in 2D *each* triangle of the discretization is refined to four smaller triangles. However, FEM meshes also allow for *adaptive* strategies where only certain elements of the triangulation are refined. The investigated solver JCMharmony uses a residuum-based error-estimator¹⁹ for adaptive grid refinement. Obviously, adaptive grid refinement is especially useful when the sought solutions are geometrically localized, or when the geometry exhibits sharp features, like discontinuities in the refractive index distribution.

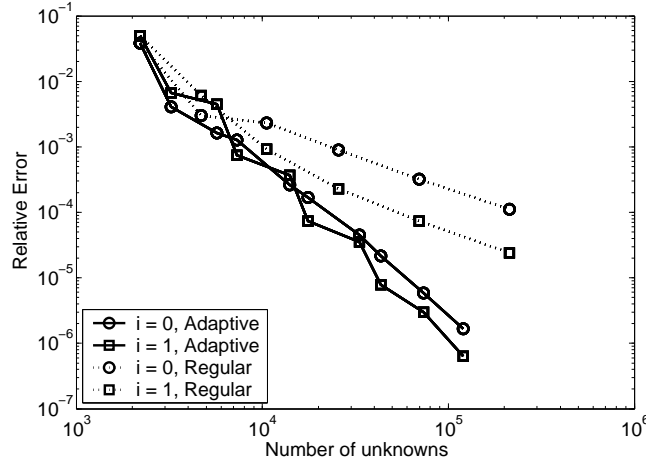


Figure 4. Comparison adaptive vs. regular FEM grid refinement. Relative error of the transmission intensity in the zero (circles) and first (squares) order of TM-polarized light incident onto a periodic line mask, calculated with the FEM solver JCMharmony. Solid lines correspond to automatic adaptive refinement, dotted lines correspond to regular refinement.

We compare the different refinement strategies by observing the convergence of the solutions obtained for increased grid resolution (i.e., increased number of unknowns). The setting is similar to the one in Section 3.2, the parameters are given in Table 1 (data set 3), and the incident light is TM-polarized. Fig. 4 shows the convergence of the relative error of the light intensity, $\Delta I = |I_{N,i} - I_{\text{inf},i}|/I_{\text{inf},i}$, in two different diffraction orders for adaptive and for regular grid refinement. Here, $I_{N,i}$ denotes the light intensity in the i^{th} diffraction order calculated from a solution with N unknowns, $I_{\text{inf},i}$ denotes the intensity calculated on a very fine grid (*quasi-exact solution*). In this example, the use of the error estimator and adaptive refinement yields two orders of magnitude in the accuracy of the error for a number of unknowns of $N \sim 10^5$.

3.4. Fully 3D Simulations

As a true 3D example, we have examined the transmission through a mask with a periodic 3D pattern as shown in Figure 6a (“chequerboard pattern”). It is illuminated by a plane wave incident from top. The parameters h , n_1 , n_2 , n_3 , and λ_0 are the same as in the previous examples. The mask is discretized by a tetrahedral mesh supporting second order Nedgelec elements.¹³ The initial triangulation is shown in Figure 6b. After two

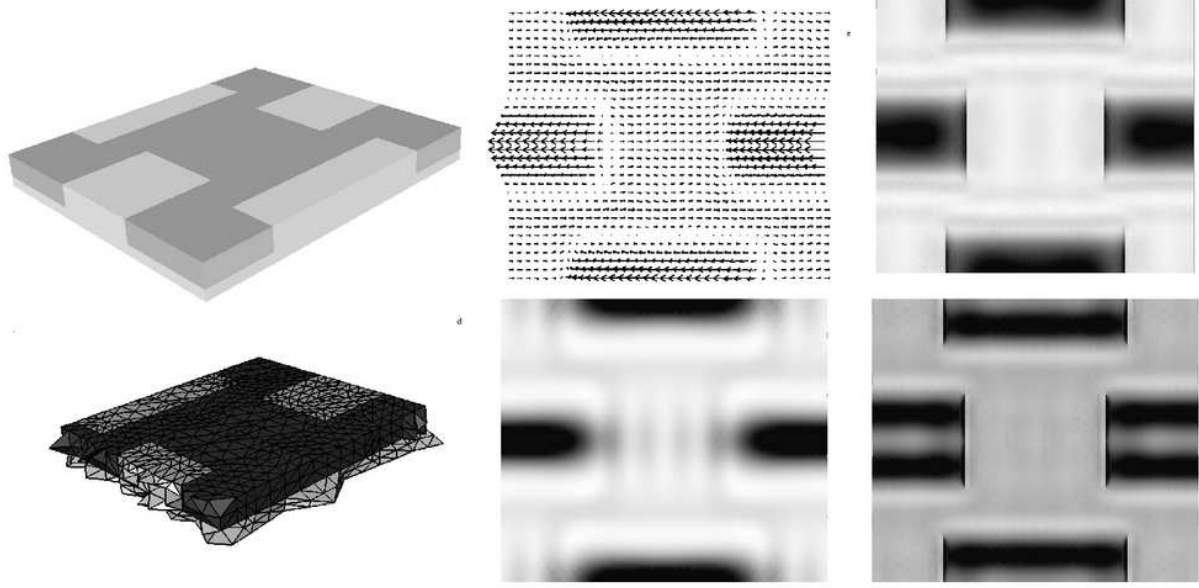


Figure 5. Unit cell ($920 \text{ nm} \times 800 \text{ nm} \times 85.4 \text{ nm}$) of a periodic mask pattern (a) built up from absorbing material (dark gray, n_1) and air (light gray) and its initial tetrahedral triangulation (b). The mask is illuminated at normal incidence. The graphs (c) and (d) show the (projected) vectorial solution and the corresponding intensity gray scale map on a cross section well below the output side of the mask, (e) and (f) show intensity maps for cross sections in the middle and at the input side of the mask, respectively (white: low intensity, black: high intensity). (See original publication for images with higher resolution.)

refinement steps, the discretization led to a linear system with $2.7 \cdot 10^6$ unknowns. A cross section of the 3D vectorial solution (c) and cross sections through the 3D intensity distribution (d-f) are also shown in Fig. 5. One clearly observes the expected discontinuous behavior of the electric field at material interfaces. For more details on 3D FEM computations we refer to a previous work.²⁰

4. BENCHMARK OF DIFFERENT RIGOROUS METHODS

We have performed a benchmark of the previously described FEM solver JCMharmony and two other advanced methods, which are also commercially available: The Finite-Difference Time-Domain solver SOLID E,²¹ and the solver Delight,⁸ which relies on a waveguide-method. In this benchmark we have investigated light propagation through a phase mask. The geometry of the problem is outlined schematically in Figure 1. A plane electromagnetic wave is incident onto the computational domain with a wavelength of λ , a wavevector of $\vec{k} = (0, 0, +2\pi/\lambda)$ and a polarization of $\vec{H} = (0, H_y, 0)$, with $H_y = n_2^{1/2} \cdot 1 \text{ A/m}$ (TM), resp. $\vec{E} = (0, E_y, 0)$, $E_y = n_2^{-1/2} \cdot 1 \text{ V/m}$ (TE). The geometrical and material parameters are denoted in Table 1 (data set 4).

For a quantitative assessment of the different simulation methods we investigate the internal convergence behavior of the simulation results, i.e., the deviation of the simulation results from the highest effort result obtained with the same method. It turns out that in all cases the accuracy of the field representation inside the computational domain dominates the convergence speed. For FDTD both space and time resolution are affected since the stability of the method requires aligning time resolution with spatial resolution. For the differential method, the spatial resolution is determined by the number of Fourier coefficients – since the grating considered here exhibits discontinuities in the material distribution, evanescent waves play an important role for correctly approximating the fields in the mask. For the FEM solver, the accuracy of the solution depends on the number of unknowns which is given by the number of geometrical patches (triangles in 2D) and by the parameters of the polynomial functions defined on the finite elements. The focus of the benchmarking is to compare the convergence speed rather than absolute runtime, i.e., the accuracy gain obtained by an increase in runtime.

JCMharmony (regular refinement, TE)				JCMharmony (regular refinement, TM)			
t[units]	$\Re(FC_0)$	$\Im(FC_0)$	$ FC_0 $	t[units]	$\Re(FC_0)$	$\Im(FC_0)$	$ FC_0 $
5.9	-0.16969573	0.24799014	0.30049251	5.9	-0.22884477	0.26037940	0.34665164
8.0	-0.15784440	0.26773822	0.31080317	8.0	-0.22041911	0.27107079	0.34937652
14.2	-0.15751644	0.26927004	0.31195799	14.2	-0.21964384	0.27189080	0.34952543
30.7	-0.15749704	0.26937915	0.31204238	30.7	-0.21950479	0.27184885	0.34940542
83.9	-0.15749576	0.26938618	0.31204780	84.5	-0.21946245	0.27181601	0.34935327
238.4	-0.15749568	0.26938662	0.31204814	239.2	-0.21944684	0.27180433	0.34933438
JCMharmony (adaptive refinement, TE)				JCMharmony (adaptive refinement, TM)			
t[units]	$\Re(FC_0)$	$\Im(FC_0)$	$ FC_0 $	t[units]	$\Re(FC_0)$	$\Im(FC_0)$	$ FC_0 $
6.1	-0.16635461	0.25218040	0.30210728	6.5	-0.22657994	0.26033139	0.34512447
8.7	-0.15969388	0.26077231	0.30578478	9.2	-0.22010390	0.26697463	0.34600748
13.7	-0.15733135	0.26825170	0.31098574	14.6	-0.22002495	0.27095147	0.34903536
21.4	-0.15753513	0.26904719	0.31177509	22.8	-0.21943271	0.27137278	0.34898982
39.1	-0.15748778	0.26931712	0.31198416	38.6	-0.21950100	0.27175820	0.34933252
63.3	-0.15749761	0.26937208	0.31203656	63.4	-0.21944800	0.27177929	0.34931563
112.7	-0.15749472	0.26938188	0.31204356	109.5	-0.21944616	0.27179933	0.34933006
185.5	-0.15749585	0.26938548	0.31204724	181.8	-0.21943960	0.27179803	0.34932493
323.9	-0.15749560	0.26938635	0.31204786	312.7	-0.21943846	0.27179904	0.34932501
549.7	-0.15749569	0.26938657	0.31204810	516.5	-0.21943773	0.27179869	0.34932427
SOLID E (TE)				SOLID E (TM)			
t[units]	$\Re(FC_0)$	$\Im(FC_0)$	$ FC_0 $	t[units]	$\Re(FC_0)$	$\Im(FC_0)$	$ FC_0 $
7.8	-0.2582035	0.2073675	0.3311651	9.1	-0.2342025	0.2523403	0.3442767
13.9	-0.2528993	0.1670695	0.3031011	13.5	-0.2512106	0.2257843	0.3377652
39.8	-0.2561597	0.1580582	0.3009986	38.6	-0.2586513	0.2177905	0.3381319
192.3	-0.2582230	0.1603459	0.3039571	170.2	-0.2572943	0.2210333	0.3391991
1178.7	-0.2607888	0.1537159	0.3027199	1103.6	-0.2622736	0.2131887	0.3379894
2109.6	-0.2610307	0.1552241	0.3036965	1938.8	-0.2609029	0.2143467	0.3376608
12169.9	-0.2621858	0.1537540	0.3039435	11785.0	-0.2618512	0.2107800	0.3361462
Delight (TE)				Delight (TM)			
t[units]	$\Re(FC_0)$	$\Im(FC_0)$	$ FC_0 $	t[units]	$\Re(FC_0)$	$\Im(FC_0)$	$ FC_0 $
2.9	-0.16846924	0.26716937	0.31585022	2.9	-0.21385244	0.24047966	0.32181258
4.0	-0.16292394	0.27139397	0.31654209	4.0	-0.21239923	0.24108101	0.32129968
5.6	-0.15993653	0.27081034	0.31451221	5.6	-0.21631258	0.24383531	0.32595520
12.0	-0.15843702	0.27004071	0.31308828	12.0	-0.21957244	0.25051824	0.33312377
23.4	-0.15802117	0.26980806	0.31267728	23.4	-0.22051428	0.25495307	0.33708696
44.4	-0.15784463	0.26971301	0.31250606	44.4	-0.22081221	0.25792098	0.33953095
124.3	-0.15770936	0.26964098	0.31237558	124.3	-0.22088603	0.26158676	0.34237154
587.0	-0.15764073	0.26960489	0.31230977	587.0	-0.22067944	0.26517225	0.34498657
1800.2	-0.15762403	0.26959612	0.31229378	1800.2	-0.22048563	0.26692949	0.34621564

Table 2. Computation times, real and imaginary parts and magnitudes of the 0^{th} Fourier coefficients $A_y(\vec{k}_{FC} = 0)$ for polarizations TE and TM and for the three benchmarked methods. Geometrical and material parameters are denoted in Table 1 (data set 4). For each method, increased computation time corresponds to a higher spatial resolution. Please note that with Delight, both, TE and TM modes are computed simultaneously, JCMharmony was used with regular and with adaptive grid refinement. Units of the Fourier coefficients are [V/m] (TE), resp. [A/m] (TM).

Therefore, other settings of the simulators were conservatively chosen in order to avoid any influence on the accuracy. This means, we expect that a more aggressive tuning of these parameters or implementations might slightly reduce the absolute runtime for all methods.

As output we monitor the coefficients of the Fourier decomposition of the solution at the output boundary of the computational domain. The square of the Fourier coefficients is proportional to the power of light diffracted into the corresponding diffraction order of the periodic mask.

The Fourier coefficient of the y -component of the investigated field $\vec{f} = \vec{E}$, resp. \vec{H} is defined as

$$A_y(\vec{k}_{FC}) = \frac{1}{p_x} \int_{-p_x/2}^{p_x/2} f_y(x, y, z_0) \exp(-i\vec{k}_{FC}\vec{x}) dx, \quad (5)$$

where \vec{k}_{FC} is the projection of the wavevector of the investigated diffraction order onto the x - y -plane ($\vec{k}_{FC} = 0$ for zero order and perpendicular incidence). Table 2 lists the Fourier coefficients for TE and TM polarization, obtained from the solutions of the three benchmarked solvers with different resolutions. JCMharmony has been used in adaptive and in regular grid refinement mode (see Section 3.3). To ease the use of Table 2, we have marked the already converged digits in bold.

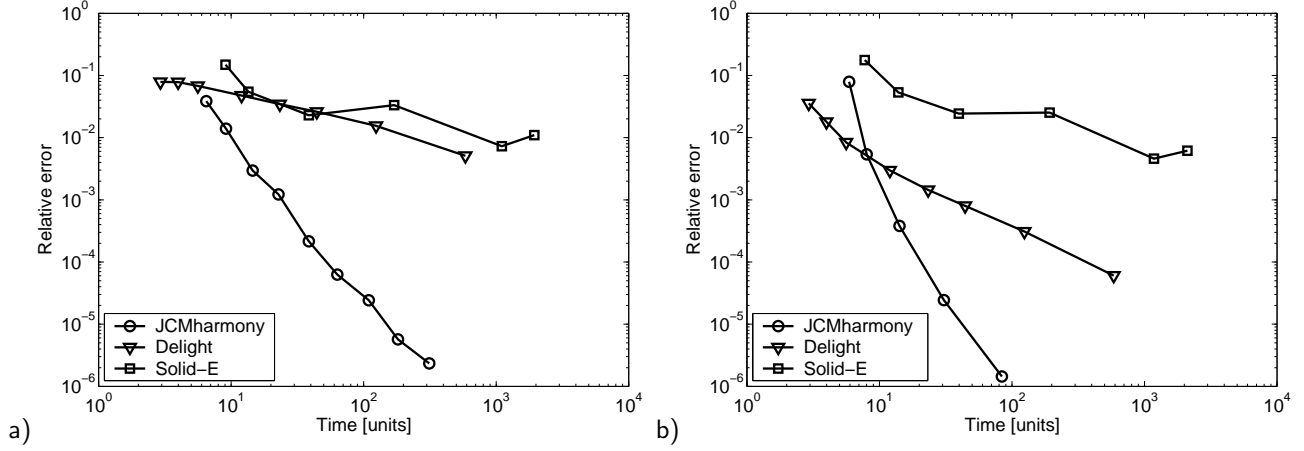


Figure 6. Relative error (ΔA_0) of the 0^{th} complex Fourier coefficient vs. normalized computation time for TM-polarization (a) and TE-polarization (b). Circles correspond to results obtained with JCMharmony (with adaptive (a), resp. regular (b) grid refinement mode), triangles to Delight and squares to SOLID E. The corresponding data is listed in Table 2.

Figure 6 shows the convergence of the different methods. Plotted is the relative error of the 0^{th} order complex Fourier coefficient, $A_y(0)$, of the simulated field components,

$$\Delta A_0 = \frac{|A_y(0) - \tilde{A}_y(0)|}{|\tilde{A}_y(0)|}, \quad (6)$$

where $\tilde{A}_y(0)$ denotes the complex Fourier coefficient computed at highest spatial resolution with the corresponding method, vs. computation time. Since the computations were carried out on different platforms, computation time is given in units of a Matlab FFT run on the same platform. One unit of time corresponds to approx. 0.25 sec on a personal computer (Intel Pentium IV, 2.5 GHz). In spite of the respective internal convergence, we observe that the intensities of the 0^{th} order diffraction computed with the three methods differ significantly ($> 2\%$), especially for TM polarization. For that reason, we benchmarked the FEM solver using an example providing an analytical solution (see Section 5). The speed of convergence of the three methods differs also significantly.

It can be seen from Fig. 6 (or, alternatively, Table 1) that the convergence behavior of the benchmarked solvers differs for TE and TM polarization. In the case of TM polarization, the FEM solver JCMharmony is the only one to reach target accuracies $\Delta A_0 < 10^{-3}$. For a low target accuracy of $\Delta A_0 > 10^{-2}$ computation times are comparable for all three solvers, for a moderate target accuracy of $\Delta A_0 \approx 2 \cdot 10^{-3}$ JCMharmony is about $100\times$ faster than Delight. SOLID E reaches an accuracy of about $\Delta A_0 \approx 10^{-2}$. For low resolutions (computation time < 10 units) the loading of the code requires a significant amount of the total computation time (for SOLID E also the loading of the GUI which takes about 6 time units). In the case of TE polarization the convergence behavior of Delight is better than in the TM case, being slightly faster than JCMharmony at low target accuracies $\Delta A_0 > 1\%$, comparable at intermediate target accuracies $\Delta A_0 \approx 1\%$, and about $20\times$ slower

than JCMharmony at high target accuracies of $\Delta A_0 \approx 10^{-4}$. Please note that in the TM case adaptive grid refinement yields a gain in convergence for the FEM solver JCMharmony, while in the TE case it is not superior to regular grid refinement (see also Section 3.3).

5. BENCHMARKING WITH AN ANALYTICAL SOLUTION

The attainable absolute accuracy of the finite element solver was assessed using an example which is close enough to lithography applications and allows for a fully vectorial 2D quasi-analytic solution by means of a series expansion with proven convergence. The geometry is depicted in Fig. 7. It consists of dense lines and spaces in an infinitely thin membrane mask of perfectly conducting metal embedded in free space. The metal layer covers the xy -plane, the strips of the grating are oriented in y -direction. The grating is illuminated from the top by a TM polarized plane wave, i.e., $H_{y,\text{in}} = \exp(-ik_z z - i\omega t)$. Geometry plus incident wave imply the following properties: (A) H_y does not depend on the y -direction which allows us to write $H_y = H_y(x, z)$, Maxwell's equations separate for the H_y -component yielding a Helmholtz equation, (B) the field is periodic in x with period $2L$, (C) the condition $H_y(x, 0) = 1$ holds true inside the gap, $|x| < a$, whereas the condition $\partial_n H_y(x, 0) = 0$ holds true outside this gap, $a < |x| < L$. Altogether, the time harmonic Maxwell's equations for the magnetic field component H_y reduce to

$$\begin{aligned} \partial_{xx} u + \partial_{zz} u + k^2 H_y &= 0 & \text{for } (x, z) \in [-L, L] \times \mathbb{R}^- \\ H_y(-L, z) &= H_y(L, z) & (\text{periodicity in } x) \\ \partial_n H_y(x, 0) &= 0 & \text{for } a \leq |x| \leq L \\ H_y(x, 0) &= 1 & \text{for } |x| \leq a \\ &+ \text{radiation condition for the scattered field.} \end{aligned}$$

Periodicity in x justifies the Fourier expansion $H_y(x, z) = \sum_{-N}^{N-1} c_n(z) \exp(in\pi x/L)$. Inserted into (7) we obtain

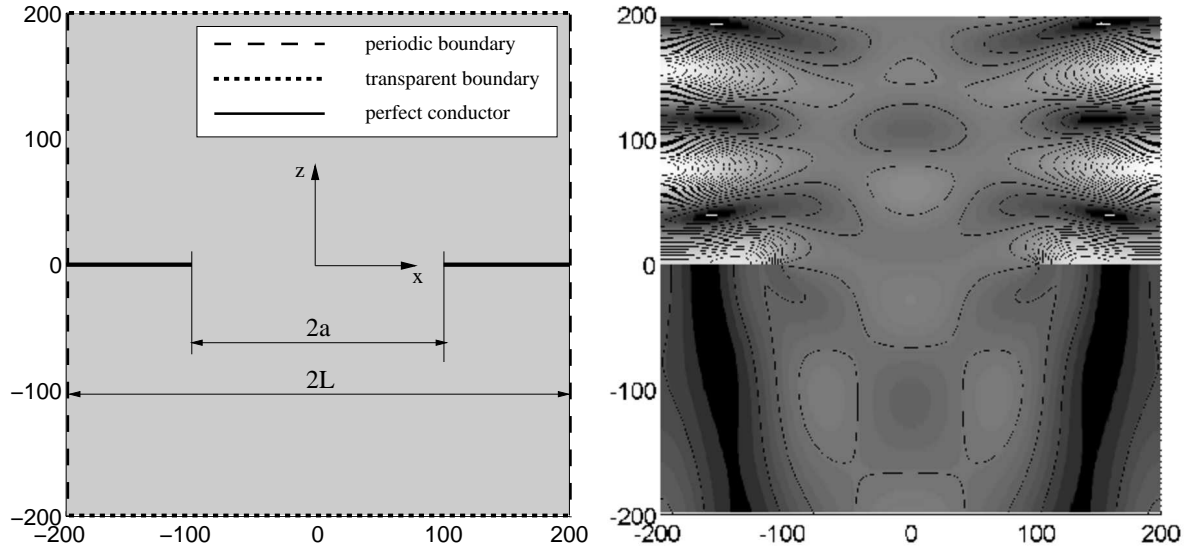


Figure 7. Left: Geometry of the problem reduced to a 2D scheme in the x, z plane. Right: Intensity plot of the superposition of incident and scattered field (black: low intensity, white: high intensity).

the ordinary differential equation $c_n''(z) = ((n\pi/L)^2 - k^2)c_n(z)$ for the unknown coefficients $c_n(z)$. It has the general solution

$$c_n(z) = \begin{cases} a_n \exp(\sqrt{(n\pi/L)^2 - k^2} z) + b_n \exp(-\sqrt{(n\pi/L)^2 - k^2} z) & \text{for } k^2 < (n\pi/L)^2 \\ a_n \exp(i\sqrt{k^2 - (n\pi/L)^2} z) + b_n \exp(-i\sqrt{k^2 - (n\pi/L)^2} z) & \text{for } (n\pi/L)^2 < k^2 \end{cases}.$$

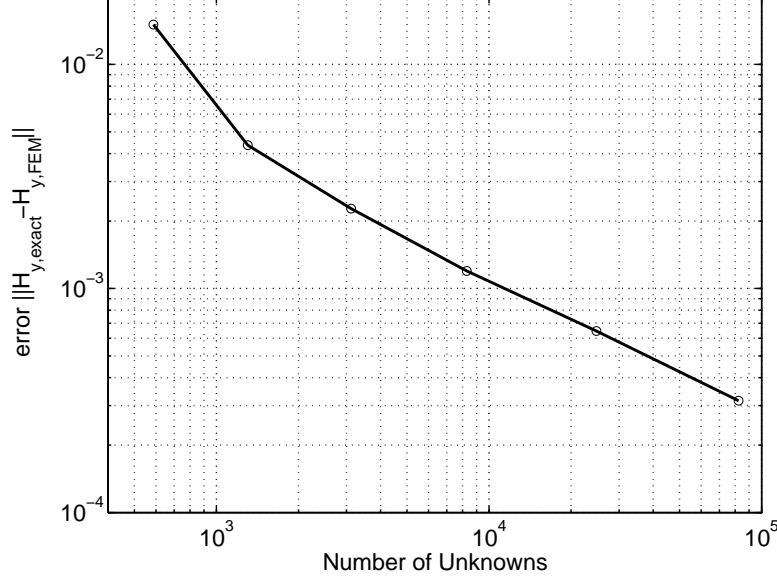


Figure 8. Convergence of the FEM approach towards the analytic solution. (See original publication for images with higher resolution.)

The coefficients a_n, b_n have to be chosen such that a proper radiation condition holds true. This implies $b_n = 0$ since we firstly require decaying solutions in case of $(n\pi/L)^2 > k^2$ and $z \rightarrow -\infty$, and secondly, outgoing solutions in case of $(n\pi/L)^2 < k^2$ and $z \rightarrow -\infty$. Based on the ansatz for H_y , the derived explicit solutions for the coefficients c_n in terms of coefficients a_n , an uniform sampling, $x_n = -L + nL/N, n = -N, \dots, N-1$, we obtain $2N$ equations for $2N$ unknowns a_n :

$$\begin{aligned} H_y(x_n, 0) = 1 &= \sum_n a_n e^{in\pi x_n/L} \quad \text{for } n \text{ such that } |x_n| \leq a \\ \partial_n H_y(x_n, 0) = 0 &= \sum_n a_n \sqrt{(n\pi/L)^2 - k^2} e^{in\pi x_n/L} \quad \text{for } n \text{ such that } a \leq |x_n| \leq L. \end{aligned}$$

The numerical solution of this system supplies the quasi-analytic reference solution $H_y(x, 0)$ with $|x| \leq L$. The reference solution was computed with $N = 2^{12}$ ensuring an error less than 10^{-6} with respect to the mean quadratic error, $\|H_{y,N} - H_{y,\text{exact}}\| := 1/N \sqrt{\sum_n (H_{y,N}(x_n) - H_{y,\text{exact}}(x_n))^2}$, on the interval $-L \leq y \leq L$ at $z = 0$. The reference solution was then compared to FEM solutions with increasing number of unknowns, where exactly the geometry depicted in Fig. 7 was used. The convergence results are presented in Fig. 8. The first FEM solution was obtained for 587 unknowns yielding an error $1.506 \cdot 10^{-2}$, the last solution was computed with 82303 unknowns yielding an error $3.158 \cdot 10^{-4}$. This proves that the FEM solver JCMharmony produces simulation results which converge to the exact solution of the scattering problem. The current implementations of the other solvers did not allow to examine this example with these.

6. CONCLUSIONS

We have benchmarked a FEM solver for mask simulations against two other rigorous methods (FDTD and waveguide method). The FEM solver allowed to reach high accuracies which were not accessible with the other methods. The computation time for phase mask simulations at moderate target accuracies was up to two orders of magnitude lower when using the FEM solver compared to the other methods. Further we have performed a benchmark of the FEM solver against an analytically accessible problem, and we have shown the wide range of applications of the solver by examining several typical simulation problems.

ACKNOWLEDGMENTS

We acknowledge financial support by the Ministry of Education and Research of the Federal Republic of Germany (Project No. 01M3154D), by the DFG Research Center MATHEON, and by the priority programme SPP 1113 of the Deutsche Forschungsgemeinschaft, DFG.

REFERENCES

1. A. Erdmann, "Process optimization using lithography simulation," *Proc. SPIE* **5401**, p. 22, 2004.
2. S. Teuber, K. Bubke, I. Höllein, R. Ziebold, and J. H. Peters, "Determination of mask induced polarization effects occurring in Hyper NA immersion lithography," *Proc. SPIE* **5754**, p. 543, 2005.
3. R. März, S. Burger, S. Golka, A. Forchel, C. Herrmann, C. Jamois, D. Michaelis, and K. Wandel, "Planar high index-contrast photonic crystals for telecom applications," in *Photonic Crystals - Advances in Design, Fabrication and Characterization*, K. B. et al., ed., pp. 308–329, Wiley-VCH, 2004.
4. S. G. Johnson and J. D. Joannopoulos, "Block-iterative frequency-domain methods for Maxwell's equations in a planewave basis," *Opt. Express* **8**(3), p. 173, 2001.
5. A. Taflov and S. Hagness, *Computational Electrodynamics: The Finite-Difference Time-Domain Method, 2nd Ed.*, Artech House, 2000.
6. A. Erdmann and C. M. Friedrich, "Rigorous diffraction analysis for future mask technology," *Proc. SPIE* **4000**, p. 684, 2000.
7. R. Petit, *Electromagnetic Theory of Gratings*, Springer-Verlag, 1980.
8. H. Kirchauer, *Photolithography Simulation*. PhD thesis, TU Vienna, 1998.
9. M. G. Moharam, "Coupled-wave analysis of two-dimensional dielectric gratings," *Proc. SPIE* **883**, p. 8/22611, 1988.
10. K. Sakoda, *Optical Properties of Photonic Crystals*, Springer-Verlag, Berlin, 2001.
11. L. Zschiedrich, R. Klose, A. Schädle, and F. Schmidt, "A new finite element realization of the perfectly matched layer method for Helmholtz scattering problems on polygonal domains in 2D," *J. Comp. Phys.*, in press, 2005.
12. T. Hohage, F. Schmidt, and L. Zschiedrich, "Solving Time-Harmonic Scattering Problems Based on the Pole Condition I: Theory," *SIAM J. Math. Anal.* **35**(1), pp. 183–210, 2003.
13. P. Monk, *Finite Element Methods for Maxwell's Equations*, Clarendon Press, Oxford, 2003.
14. S. Burger, R. Klose, A. Schädle, F. Schmidt, and L. Zschiedrich, "FEM modelling of 3d photonic crystals and photonic crystal waveguides," in *Integrated Optics: Devices, Materials, and Technologies IX*, Y. Sidorin and C. A. Wächter, eds., **5728**, pp. 164–173, Proc. SPIE, 2005.
15. L. Zschiedrich, S. Burger, R. Klose, A. Schädle, and F. Schmidt, "JCMmode: An adaptive finite element solver for the computation of leaky modes," in *Integrated Optics: Devices, Materials, and Technologies IX*, Y. Sidorin and C. A. Wächter, eds., **5728**, pp. 192–202, Proc. SPIE, 2005.
16. O. Schenk *et al.*, "Parallel sparse direct linear solver PARDISO." Department of Computer Science, Universität Basel.
17. P. Deuffhard, F. Schmidt, T. Friese, and L. Zschiedrich, *Adaptive Multigrid Methods for the Vectorial Maxwell Eigenvalue Problem for Optical Waveguide Design*, pp. 279–293. Mathematics - Key Technology for the Future, Springer-Verlag, Berlin, 2003.
18. M. Lassas and E. Somersalo, "On the existence and convergence of the solution of PML equations.," *Computing No.3, 229-241* **60**(3), pp. 229–241, 1998.
19. V. Heuveline and R. Rannacher, "A posteriori error control for finite element approximations of elliptic eigenvalue problems," *J. Adv. Comp. Math.* **15**, p. 107, 2001.
20. S. Burger, L. Zschiedrich, R. Klose, A. Schädle, F. Schmidt, C. Enkrich, S. Linden, M. Wegener, and C. M. Soukoulis, "Numerical investigation of light scattering off split-ring resonators." *Proc. SPIE* **5955**, pp. 18–26, 2005.
21. C. Kalus, S. List, A. Erdmann, R. Gordon, M. McCallum, and A. Semmler, "Benchmarking of available rigorous electromagnetic field simulators for phase-shift mask applications," *Microelectronic engineering* **57**, p. 79, 2001.